



AFRL-RZ-WP-TP-2010-2246

**LASER-BASED MEASUREMENTS OF OH,
TEMPERATURE, AND WATER VAPOR
CONCENTRATION IN A HYDROCARBON-FUELED
SCRAMJET (POSTPRINT)**

Mark R. Gruber and Campbell D. Carter

**Propulsion Sciences Branch
Aerospace Propulsion Division**

Michael D. Ryan

Universal Technology Corporation

Gregory B. Rieker, Jay B. Jeffries, and Ronald K. Hanson

Stanford University

Jiwen Liu

Taitech, Inc.

Tarun Mathur

Innovative Scientific Solutions, Inc.

JULY 2008

Approved for public release; distribution unlimited.

See additional restrictions described on inside pages

STINFO COPY

**AIR FORCE RESEARCH LABORATORY
PROPULSION DIRECTORATE
WRIGHT-PATTERSON AIR FORCE BASE, OH 45433-7251
AIR FORCE MATERIEL COMMAND
UNITED STATES AIR FORCE**

REPORT DOCUMENTATION PAGE				<i>Form Approved</i> OMB No. 0704-0188	
The public reporting burden for this collection of information is estimated to average 1 hour per response, including the time for reviewing instructions, searching existing data sources, gathering and maintaining the data needed, and completing and reviewing the collection of information. Send comments regarding this burden estimate or any other aspect of this collection of information, including suggestions for reducing this burden, to Department of Defense, Washington Headquarters Services, Directorate for Information Operations and Reports (0704-0188), 1215 Jefferson Davis Highway, Suite 1204, Arlington, VA 22202-4302. Respondents should be aware that notwithstanding any other provision of law, no person shall be subject to any penalty for failing to comply with a collection of information if it does not display a currently valid OMB control number. PLEASE DO NOT RETURN YOUR FORM TO THE ABOVE ADDRESS.					
1. REPORT DATE (DD-MM-YY) July 2008		2. REPORT TYPE Conference Paper Postprint		3. DATES COVERED (From - To) 01 August 2007 – 21 July 2008	
4. TITLE AND SUBTITLE LASER-BASED MEASUREMENTS OF OH, TEMPERATURE, AND WATER VAPOR CONCENTRATION IN A HYDROCARBON-FUELED SCRAMJET (POSTPRINT)				5a. CONTRACT NUMBER In-house	
				5b. GRANT NUMBER	
				5c. PROGRAM ELEMENT NUMBER 62203F	
6. AUTHOR(S) Mark R. Gruber and Campbell D. Carter (AFRL/RZAS) Michael D. Ryan (Universal Technology Corporation) Gregory B. Rieker, Jay B. Jeffries, and Ronald K. Hanson (Stanford University) Jiwen Liu (Taitech, Inc.) Tarun Mathur (Innovative Scientific Solutions, Inc.)				5d. PROJECT NUMBER 3012	
				5e. TASK NUMBER AI	
				5f. WORK UNIT NUMBER 3012AI00	
7. PERFORMING ORGANIZATION NAME(S) AND ADDRESS(ES) Propulsion Sciences Branch (AFRL/RZAS) Aerospace Propulsion Division Air Force Research Laboratory, Propulsion Directorate Wright-Patterson Air Force Base, OH 45433-7251 Air Force Materiel Command, United States Air Force ----- Universal Technology Corporation Dayton, OH 45432				8. PERFORMING ORGANIZATION REPORT NUMBER AFRL-RZ-WP-TP-2010-2246 ----- Taitech, Inc. Beavercreek, OH 45430 ----- Innovative Scientific Solutions, Inc. Dayton, OH 45440	
9. SPONSORING/MONITORING AGENCY NAME(S) AND ADDRESS(ES) Air Force Research Laboratory Propulsion Directorate Wright-Patterson Air Force Base, OH 45433-7251 Air Force Materiel Command United States Air Force				10. SPONSORING/MONITORING AGENCY ACRONYM(S) AFRL/RZAS	
				11. SPONSORING/MONITORING AGENCY REPORT NUMBER(S) AFRL-RZ-WP-TP-2010-2246	
12. DISTRIBUTION/AVAILABILITY STATEMENT Approved for public release; distribution unlimited.					
13. SUPPLEMENTARY NOTES Conference paper published in the <i>Proceedings of the 44th AIAA/ASME/SAE/ASEE Joint Propulsion Conference and Exhibit</i> , conference held July 21 - 23, 2008, in Hartford, CT. Paper contains color. PA Case Number: WPAFB 08-3868; Clearance Date: 27 June 2008. The U.S. Government is joint author of this work and has the right to use, modify, reproduce, release, perform, display, or disclose the work.					
14. ABSTRACT Two laser-based measurement techniques are implemented in a direct-connect hydrocarbon-fueled scramjet combustor. Planar laser-induced fluorescence (PLIF) of the OH radical is used to examine the flame structure within the combustor. Tunable diode laser-based absorption spectroscopy (TDLAS) is used to measure water vapor concentration and static temperature near the combustor exit. Combined with conventional measurements and Reynolds-averaged CFD simulations, these optical diagnostic techniques significantly enhance the information that is obtained from the scramjet combustor. Wall pressure data show the combustor to be operating in dual-mode with two regions of elevated pressure corresponding to the primary and secondary flameholding zones. The OH radical is well-distributed across the combustor with high OH concentrations occurring along the body, side, and cowl walls. TDLAS measurements indicate non-uniform body-to-cowl profiles in both temperature and water concentration. Near-wall regions are found to be the hottest while the core region is cooler.					
15. SUBJECT TERMS supersonic combustion, laser-based diagnostics, diode lasers, PLIF					
16. SECURITY CLASSIFICATION OF:			17. LIMITATION OF ABSTRACT: SAR	18. NUMBER OF PAGES 24	19a. NAME OF RESPONSIBLE PERSON (Monitor) Mark R. Gruber 19b. TELEPHONE NUMBER (Include Area Code) N/A
a. REPORT Unclassified	b. ABSTRACT Unclassified	c. THIS PAGE Unclassified			

Laser-Based Measurements of OH, Temperature, and Water Vapor Concentration in a Hydrocarbon-Fueled Scramjet

Mark Gruber^{*} and Campbell Carter^{*}

Air Force Research Laboratory, Wright-Patterson AFB, Ohio 45433

Michael Ryan[†]

Universal Technology Corporation, Dayton, Ohio 45432

Gregory B. Rieker,[‡] Jay B. Jeffries,[§] and Ronald K. Hanson^{**}

Stanford University, Stanford, California 94305

Jiwen Liu^{††}

Taitech, Inc., Beavercreek, Ohio 45430

and

Tarun Mathur^{‡‡}

Innovative Scientific Solutions, Inc., Dayton, Ohio 45440

In this investigation, two laser-based measurement techniques are implemented in a direct-connect hydrocarbon-fueled scramjet combustor. Planar laser-induced fluorescence (PLIF) of the OH radical is used to examine the flame structure within the combustor. Tunable diode laser-based absorption spectroscopy (TDLAS) is used to measure water vapor concentration and static temperature near the combustor exit. Combined with conventional measurements and Reynolds-averaged CFD simulations, these optical diagnostic techniques significantly enhance the information that is obtained from the scramjet combustor. In this study, wall pressure data show the combustor to be operating in dual-mode with two regions of elevated pressure corresponding to the primary and secondary flameholding zones. The OH radical is well-distributed across the combustor with high OH concentrations occurring along the body, side, and cowl walls. TDLAS measurements indicate non-uniform body-to-cowl profiles in both temperature and water concentration. Near-wall regions are found to be the hottest while the core region is cooler. Similarly, the highest concentrations of water vapor are found near the walls. In general, CFD results compare well with the experimental data, although there are dissimilarities that are probably related to turbulence and chemistry sub-models within the CFD code.

Nomenclature

A	=	area
d	=	injector diameter
E	=	total energy flow
F	=	load cell force

^{*} Senior Aerospace Engineer, AFRL/RZAS. Associate Fellow.

[†] Post-Doctoral Fellow, AFRL/RZAS. Member.

[‡] Graduate Student, Department of Mechanical Engineering. Member.

[§] Senior Research Engineer, Department of Mechanical Engineering. Associate Fellow.

^{**} Professor, Department of Mechanical Engineering. Fellow.

^{††} Senior Research Scientist. Associate Fellow.

^{‡‡} Research Engineer. Senior Member.

h	=	enthalpy
H	=	engine throat height
k	=	turbulent kinetic energy
KE	=	kinetic energy flow
mom_i	=	momentum components
MW	=	molecular weight
P	=	pressure
P_{P0}	=	combustion heater total pressure
Pr_i	=	turbulent Prandtl number
Q	=	heat loss
R_u	=	universal gas constant
Sc_t	=	turbulent Schmidt number
ST	=	stream thrust
T	=	temperature
T_{VH}	=	combustion heater total temperature
U	=	velocity
V_c	=	velocity correction term in separated flow average
W	=	mass flow rate
x	=	streamwise coordinate ($x = 0$ at engine throat)
x_{H2O}	=	water vapor mole fraction
x_{CO2}	=	carbon dioxide mole fraction
y	=	transverse coordinate ($y = 0$ at cowl wall upstream of cowl step flameholder)
z	=	spanwise coordinate ($z = 0$ at spanwise centerline)
Y_F	=	frozen fuel mass fraction
α	=	injection angle relative to combustor wall
ε	=	dissipation
ϕ	=	fuel-air equivalence ratio
η_a	=	area correction term in separated flow average
$\eta_{c,AT}$	=	combustion efficiency based on temperature rise
$\eta_{c,CFD}$	=	combustion efficiency based on static enthalpy
$\eta_{c,YF}$	=	combustion efficiency based on frozen fuel
λ	=	wavelength
ρ	=	density

Subscripts

4	=	facility nozzle exit station
5	=	combustor exit station
amb	=	ambient
A	=	air stream (includes air, make-up oxygen, and combustion heater fuel)
$base$	=	combustor base
$B2$	=	B2 injection site
$B6$	=	B6 injection site
$C3$	=	C3 injection site
F	=	fuel stream
i	=	species or component reference
$ideal$	=	ideal condition
ref	=	reference condition
T	=	total or stagnation

I. Introduction

In ground tests of scramjet combustors, measurements of performance and operability are commonly made using wall-based sensors (e.g., pressure transducers, thermocouples, etc.) and either thrust (via a thrust stand) or total heat release (via calorimetry). While crucial for understanding many aspects of the combustor, these tools do not provide any information about the flowfield or the reaction zone within the flowpath. In-stream laser-based measurements in these combustors are difficult to obtain because of the harsh environment and the challenges

associated with optical access. However, optical measurement techniques offer the potential to explore many features of the combustion zone including the instantaneous and time-averaged reaction zone structure, the spatial uniformity of the flame, the extent of flame propagation across or around the flowpath, and the distribution of certain chemical species and static temperature. These techniques often require large optical windows for transmitting and/or collecting radiation from a wide range of wavelengths (from infrared to ultraviolet) in addition to ample laboratory space for mounting lasers, optics, and camera components.

Planar laser-induced fluorescence (PLIF) techniques have been applied to flowfields relevant to scramjet combustors to study hydrogen combustion in a supersonic crossflow¹ and mixing and combustion phenomena in fuel injection experiments.²⁻⁴ Donbar, et al.⁵ applied PLIF of the OH radical to the region near a cavity-based flameholder in a hydrocarbon-fueled scramjet combustor. In this study, the role of sidewall interaction was observed to be important in understanding the flame propagation mechanism across the combustor. The present work is a follow-on to this effort with the interrogation plane located downstream of a rearward facing step flameholder in a hydrocarbon-fueled scramjet combustor.

Recent proliferation of diode laser technology in the telecommunications industry has provided robust tools for diode laser-based absorption spectroscopy for both ground and flight measurements in reacting flows. Allen, et al. developed a water vapor / temperature / velocity sensor based on diode lasers for use in high-speed reacting flows.⁶ Additional refinements have been made by Liu, et al.,⁷⁻⁹ Rieker, et al.,^{10,11} and Williams, et al.^{11,12} relative to making routine quantitative measurements of water and oxygen concentration, temperature, and velocity in scramjet engines and other environments. These tools offer the potential for making high-frequency (kHz) in-stream measurements of temperature, velocity, species concentration, and pressure in reacting flows. Typically these measurements represent integrated quantities along the path of the laser line, but multiple laser lines can be employed to obtain tomographic information about the non-uniform flow.¹²

In the current work, a hydrocarbon-fueled supersonic combustor is operated in a direct-connect research facility. The combustor performance and operability characteristics are examined using conventional and advanced optical instrumentation techniques. Wall pressure and temperature measurements reveal the general operating characteristics of the combustor. Thrust measurements and a one-dimensional analysis routine provide performance estimates. PLIF of the OH radical reveals the flame structure within the combustor. Tunable diode laser-based absorption spectroscopy (TDLAS) yields quantitative measurements of static temperature and water vapor concentration near the combustor exit. In addition, reacting-flow computational fluid dynamics (CFD) simulations provide useful information for comparison with the various experimental measurements. Together, these diagnostic measurements and models provide new information toward our goal of better understanding the performance and operability of the research scramjet combustor.

II. Experimental Resources

The research combustor flowpath studied in this investigation is integrated into a continuous-flow supersonic combustion research facility capable of simulating flight conditions from Mach 3.5 to 7. This facility is supplied with air at up to 13.6 kg/s (30 lbm/s), 5.2 MPa (750 psia), and 922 K (1660°R), as well as 20.7 kPa (3.0 psia) continuous exhaust. Compressed natural gas is used to fuel the in-stream combustion heater and a liquid oxygen system provides make-up oxygen to the combustion-heated air stream. Liquid and gaseous hydrocarbon fuel systems deliver fuel to the research combustor. An electric fuel heater provides combustor fuel at the required temperatures for various simulation conditions. A recirculating cooling water system provides 9460 lpm (2500 gpm) at 483 kPa (70 psia); raw dump water at 2.4 MPa (350 psia) is also available. The entire flowpath is secured to a thrust stand for direct measurements of the thrust generated by the combustor. This measurement is combined with wall static pressure measurements and a performance analysis routine to deduce combustion efficiency and other performance parameters. Additional details about the facility are presented elsewhere.¹⁴

A. Combustor Flowpath and Fuel Delivery

A research combustor with a flush-wall fuel injection system and wall-based flameholding was used in this investigation and is shown in Figure 1. The flowpath width was constant at 229 mm (9 in.) and the reference height at the combustor entrance was 42.3 mm (1.664 in.). Removable panels in the sidewalls enabled either optical access or conventional instrumentation. The combustor had several fuel injection sites on both body and cowl sidewalls (details of the sites used in this investigation are shown in Table 1). Each injection site had a dedicated fuel supply manifold that was equipped with pressure and temperature instrumentation. Flameholding was provided by a wall

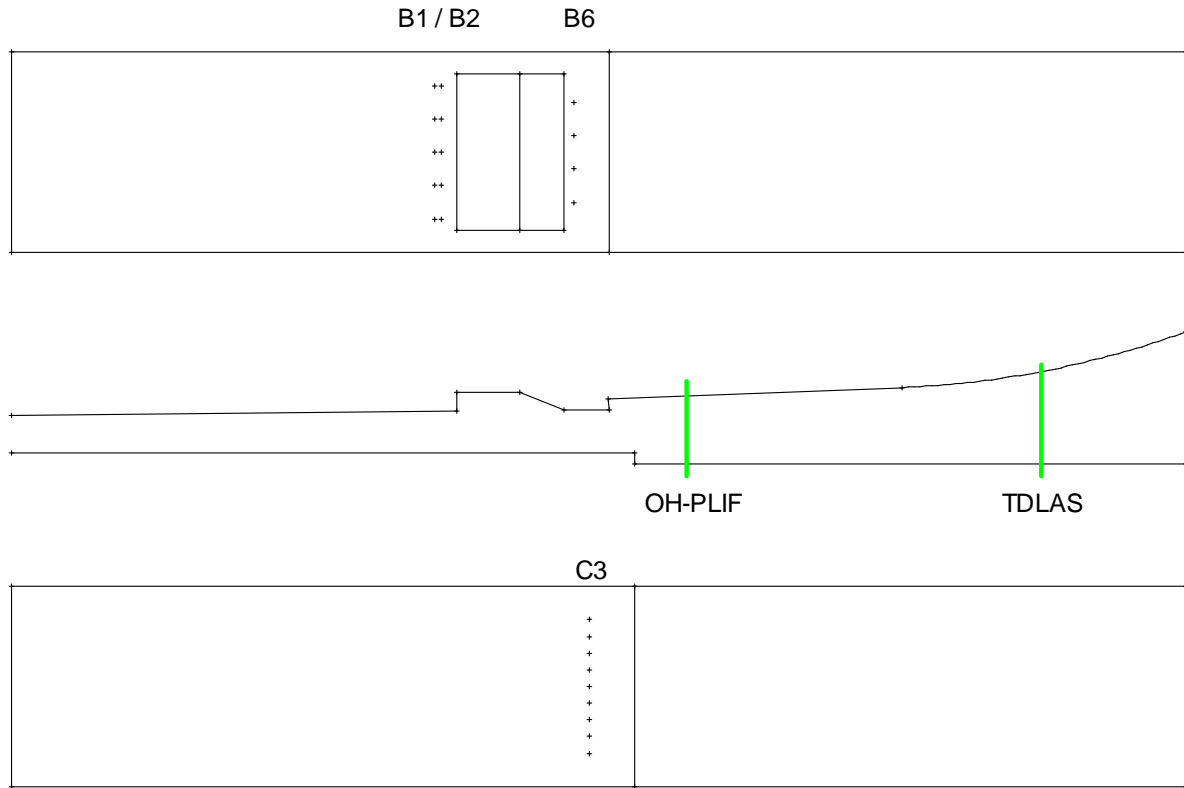


Figure 1. Flowpath schematic showing measurement planes (flow direction is left to right).

cavity and a rearward-facing step on the body side in addition to a rearward-facing step on the cowl side. The cavity had a depth of 21.6 mm (0.85 in.), a length (measured from the separation corner to the mid-ramp location) of 96.3 mm (3.79 in.), and a 22 deg. ramp angle. It spanned the central 178 mm (7 in.) of the combustor. The body-side step flameholder was 12.2 mm (0.48 in.) deep and was positioned at $x/H = 16.1$. The cowl-side step flameholder was 12.7 mm (0.50 in.) deep and was positioned at $x/H = 16.8$. The water-cooled flowpath had several access ports in the walls for optical diagnostics.

Interchangeable facility nozzles are used to generate appropriate supersonic flow conditions upstream of the combustor flowpath. In this investigation, a Mach 2.84 nozzle/distortion generator assembly was used to simulate Mach 5 – 5.5 flight conditions. Prior to combustion experiments, a series of calibrations was performed using a water-cooled traversing pitot pressure/stagnation temperature probe and wall-based measurements.¹⁵ The research combustor was installed as shown in Figure 2.

Table 1. Fuel injector details.

	B1	B2	B6	C3
Number	5	5	4	9
d (mm)	3.96	3.96	2.36	2.36
α (deg.)	30	90	90	90
Spacing (mm)	38.1	38.1	38.1	19.0

The fuel control system was comprised of several devices designed to control both the total fuel flow rate and the distribution of fuel among the desired fuel injection sites. One of two Coriolis mass flow meters (Rheonik model RHM20 or RHM08, depending on the total fuel flow rate) was used to meter the supply of room-temperature fuel delivered to the combustor and to provide feedback to the primary control valve that maintained the desired overall equivalence ratio. The fuel then flowed into two fuel

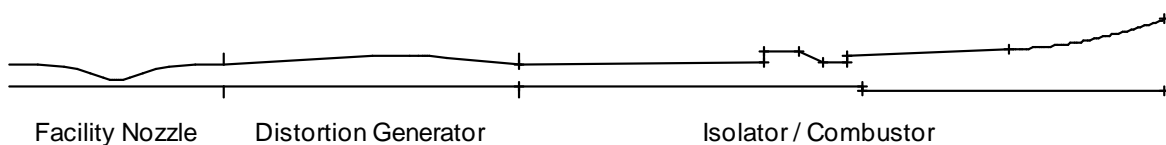


Figure 2. Hardware installation (flow direction is left to right).

manifolds, one supplying the body-side injectors and the other supplying the cowl-side injectors. A second control valve was used to regulate the fuel flow rate to the primary injection site (either B1 or B2). The remaining fuel was then routed to the secondary injection sites. Sonic nozzles were used to set the fuel distribution delivered to these injectors. All of the fuel injection sites were calibrated prior to combustion testing to determine discharge coefficients. This information was used in conjunction with the measured injector areas and measured fuel properties in the injector manifolds to determine the actual fuel distribution delivered to the combustor.

B. Instrumentation, Analyses, and Measurement Uncertainties

A CAMAC-based data acquisition and control system had 480 channels of analog input, 64 channels of digital I/O, and 40 channels of analog output. The CAMAC crates were connected to a Linux workstation via a fiber optic Grand-Interconnect interface for both control and data acquisition. A Pressure Systems Incorporated (PSI) 8400 pressure scanning system consisting of 400 channels with real-time display and data reduction was also used. The facility nozzle had 30 static pressure ports on its cowl wall. The distortion generator had 25 pressure taps on its cowl wall. The combustor had over 200 pressure taps instrumented on all four walls, including measurements at the combustor exit and in the base areas of each wall. A large array of thermocouples was used to monitor air, fuel, oxygen, cooling water, and hardware wall temperatures. The water temperatures, along with measured water flow rates, were used to compute the heat losses from the various components. In addition, all flows (air, fuels, water, and oxygen) were measured using orifice plates, turbine flow meters, Coriolis mass flow meters, or Venturi flow meters. Several video cameras provided remote visual monitoring of the tests.

An in-house code (QPERF) is used to calculate combustor performance. This code was validated against the industry-standard codes RJPA and GASL-1D.¹⁶ QPERF solves the one-dimensional conservation equations shown in Eqs. 1-3 applied to the control volume shown in Figure 3 using the measurements of the reactant mass flow rates, load cell force, heat loss, base pressure, exit pressure, and ambient pressure.

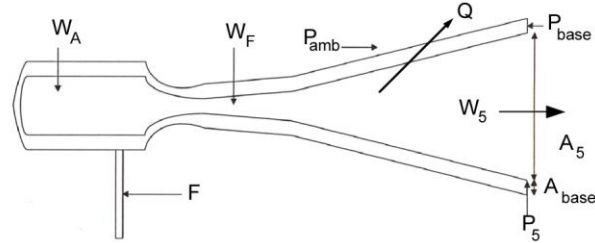


Figure 3. Control volume for QPERF analysis.

$$\rho_5 U_5 A_5 = W_A + W_F = W_5 \quad (1)$$

$$W_5 U_5 + P_5 A_5 = ST_5 = F + P_{amb} A_5 + (P_{amb} - P_{base}) A_{base} \quad (2)$$

$$W_5 \left(h_5 + \frac{1}{2} U_5^2 \right) = W_A \left(h_A + \frac{1}{2} U_A^2 \right) + W_F \left(h_F + \frac{1}{2} U_F^2 \right) - Q \quad (3)$$

Reactant enthalpies are determined from the measured reactant temperatures. There are four remaining unknowns: exit density (ρ_5), exit enthalpy (H_5), exit velocity (U_5), and mass fraction of frozen or unburned fuel (Y_F). Equation 2 then yields the relationship shown in Eq. 4 for U_5 .

$$U_5 = \left(\frac{ST - PA}{W} \right)_5 \quad (4)$$

Equation 4 is substituted into Eqs. 1 and 3 to yield ρ_5 and H_5 , respectively. A value for Y_F is initially selected and fed into a chemical equilibrium package using the known exit pressure and total enthalpy (from Eq. 3) to yield the temperature and molecular weight of the mixture. Then the exit density is found from the equation of state (Eq. 5).

$$\rho_5 = \left(\frac{P \cdot MW}{R_u \cdot T} \right)_5 \quad (5)$$

A Newton's iteration is used to vary Y_F until the density from Eq. 5 matches that determined from Eq. (1) to within the prescribed convergence criteria. Once Y_F is known, the equilibrium code is used to compute the exit total temperature. Repeating the equilibrium calculation and setting Y_F to 1.0×10^{-6} yields the ideal total temperature. The total temperature at the facility nozzle exit is found by performing another equilibrium calculation on the combustion heater flow assuming all of the combustion heater fuel is consumed. Finally, two measures of combustor efficiency are computed using either the mass fraction of frozen fuel (Eq. 6), or the combustor temperature rise (Eq. 7). In this paper, all combustion efficiency values are based on the mass fraction of frozen fuel.

$$\eta_{c,YF} = 1 - Y_F, \phi \leq 1$$

$$\eta_{c,YF} = (1 - Y_F)\phi, \phi > 1$$
(6)

$$\eta_{c,\Delta T} = \frac{T_{T5} - T_{T4}}{T_{T5,ideal} - T_{T4}}$$
(7)

An extensive uncertainty analysis has recently been completed for the research facility.¹⁷ Typical results from this analysis for several performance parameters are shown in Table 2. All values in the table are presented as percent of reading.

C. Planar Laser-Induced Fluorescence of the Hydroxyl Radical (OH-PLIF)

OH-PLIF was used to obtain spatially and temporally resolved images of the reaction zone within the scramjet combustor. OH is an intermediate combustion species that serves as an indicator of high-temperature regions associated with the flame and the burnt gases. The OH-PLIF set-up is shown in Figure 4. The second harmonic of a 10-Hz Spectra Physics GCR-170 Nd:YAG laser was used to pump a Lumonics Hyperdye dye laser. The resulting dye laser beam was then frequency doubled using an Inrad Autotracker III to produce ~10 mJ/pulse at 283.5 nm. The doubled 567-nm dye beam matched the wavelength for the Q₁(8) transition of the A²Σ⁺←X²Π (1,0) band of OH. The desired pump beam was separated from the fundamental dye beam by way of a prism-based harmonic separator. A small portion of the beam was directed over a reference flame and then to a fast photodiode by way of a fused-silica flat to enable constant monitoring of laser tuning and pulse energy. The sheet was formed by first sending the beam through a -5-cm focal length plano-concave fused silica lens then through a 1-m focal length biconvex spherical fused silica lens; this telescope provided a well-expanded laser sheet that was reasonably uniform in irradiance over the entire combustor height. Limited optical access to the combustor resulted in sending the beam through the same window through which the camera viewed the fluorescence. The focusing lens and final turning mirror were located on a translation table as was the camera, enabling translation of the probe region; however, for these measurements the probe plane location was maintained at 5.7 cm downstream of the cowl-side step.

The camera was a Roper Scientific PI-Max intensified CCD camera (512×512 pixel array) with a Superblue photocathode; the pixels were binned 2×2 before readout so that the camera could achieve a 10 frame/s readout, thus matching the laser repetition rate. The intensifier was gated to 100 ns for each exposure; additionally the intensifier's micro-channel plate was gated to further reduce the strong flame emission. The Cerco 45-mm focal length, f/1.8 UV lens was placed on a Scheimpflug mount so that focus was maintained across the camera field of view. UG5 and WG305 Schott glass filters were placed on the lens to allow detection of the A-X (v'=1, v''=1) and (0,0) band fluorescence—where the v'=0 level is populated through vibrational energy transfer—while blocking laser scattering, (1,0) band fluorescence, and background flame luminosity. Due to the limited optical access, the camera was only able to view the half of the combustor closest to the window. An example OH-PLIF image with the respective geometry is shown in Figure 5. A series of 200 images was taken for each fueling condition, after combustion had reached a steady state. The first 20 images of that sequence were taken with the laser shuttered off for background luminosity subtraction. The images were de-warped, i.e., corrected for perspective distortion, using a projective transformation after determining the field of view by imaging a grid of dots at the laser plane.

Table 2. Measurement uncertainties.

Parameter	Uncertainty (%)
$\eta_{c,YF}$	± 4.2
ST_5	± 1.0
W_A	± 4.0
W_F	± 0.6
Q	± 4.7
P_{base}	± 0.1
P_{amb}	± 0.4
P_5	± 0.1
F	± 2.9

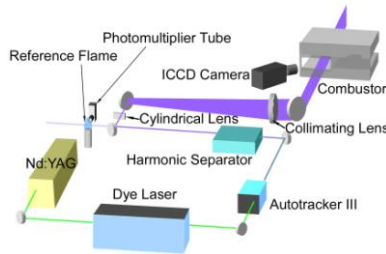


Figure 4. OH-PLIF set-up.

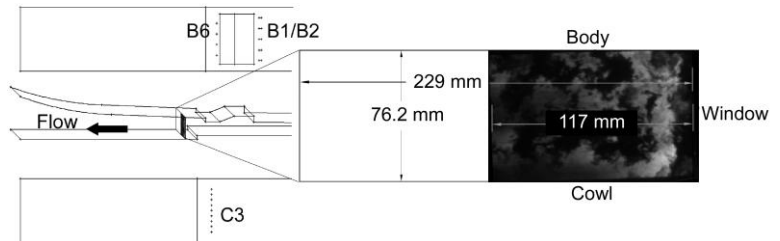


Figure 5. Combustor geometry showing image plane.

D. Tunable Diode Laser-Based Absorption Spectroscopy

The line-of-sight temperature and water vapor concentration measurements are based on TDLAS using near-IR telecommunications lasers. Wavelength modulation spectroscopy with second harmonic detection (WMS-2f) is used because it offers increased resistance to noise over traditional direct absorption techniques. Improved WMS-2f models and normalization of the WMS-2f signal by the first harmonic (1f) signal enable calibration-free WMS measurements.^{18,19} In addition, 1f-normalization provides resistance to perturbations in laser transmission (window fouling, scattering, etc.).^{20,21} Gas temperature is determined by the ratio of 1f-normalized WMS-2f signals from two spectral features with different temperature-dependent absorption characteristics. Water vapor concentration is determined from the 1f-normalized WMS-2f signal in conjunction with the previously determined gas temperature.¹⁸

Figure 6 shows a schematic of the TDLAS setup used for these measurements. Two distributed-feedback (DFB) diode lasers with output wavelengths centered on different absorption features of water vapor are fiber-multiplexed and carried to the scramjet combustor exit via single mode optical fiber. The light is collimated with an aspheric lens and passed across the scramjet combustor exit. The light is then captured with a 9.9-mm diameter lens and focused into a 400-micron multimode fiber. A

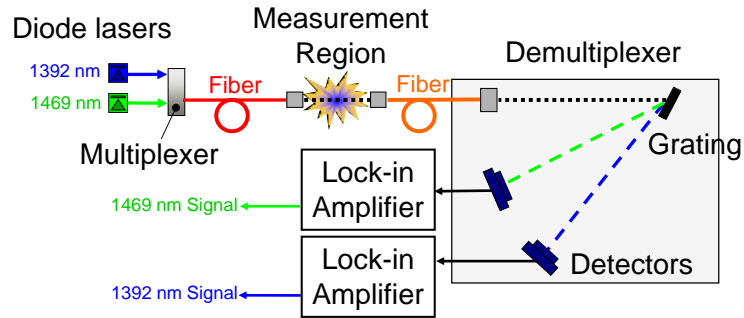


Figure 6. Schematic of TDLAS sensor for temperature and water vapor concentration.

grating-based demultiplexer separates the light onto two 3-mm diameter InGaAs detectors. The data acquisition system has been configured to allow continuous data acquisition at 2.5 MHz for up to 5 hours. The detector signals are post-processed with a software lock-in amplifier to recover the WMS-1f and WMS-2f signals.

The TDLAS sensor utilizes the spectral feature at 1391.67 nm (7185.60 cm^{-1}) with lower state energy 1045 cm^{-1} and the spectral feature at 1468.89 nm (6807.83 cm^{-1}) with lower state energy 3219 cm^{-1} . The spectral parameters (line strength, H_2O -, CO_2 -, air-broadening coefficients and temperature exponents), which describe the absorption characteristics of these features and are contained in the WMS models used to infer temperature and water concentration, were measured in the laboratory. The sensor was then validated against known temperatures from 600 K to 1515 K in a high-uniformity tube furnace and a uniform flat-flame burner (results of these experiments are shown in Figure 7. The standard deviation of the temperature and H_2O concentration measurements from the actual values were 4.2% and 2.7%, respectively.

The temperature measured by line-of-sight (LOS) laser absorption techniques is path-integrated in nature. For uniform temperature environments, the laser-measured temperature is identical to the gas temperature along the laser

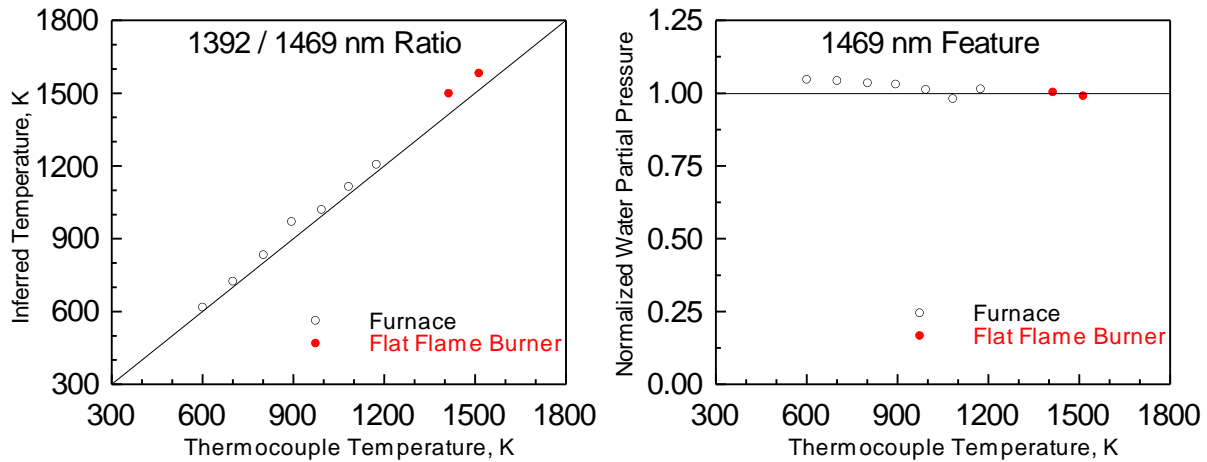


Figure 7. Temperature and water vapor partial pressure measurements in uniform environments.

beam path. For non-uniform environments, the laser-measured temperature is similar to the path-average temperature, but as shown by Seitzman and Scully,²² the LOS measurement is weighted by the temperature dependence of the probed spectral feature line strength and variation in the partial pressure of H_2O along the path. For example, absorption features that are strongest at low temperature are more affected by cold non-uniformities along the beam path than absorption features that are strongest at high temperature. Therefore, using different absorption features to probe the same non-uniform path will yield different laser-measured temperatures.^{21,22} This characteristic of absorption was utilized by Sanders et al.²³ and later by Liu et al.²⁴ to develop methods to extract non-uniform temperature profiles from LOS direct absorption measurements on up to 16 spectral features. In one method, the path is discretized into “n” unknown property “bins” (temperature, concentration, pressure, and/or path length), where n is equal to the number of probed spectral features. A matrix is built with the known spectral parameters and measured integrated absorbance values for each feature and solved for the unknown property bins. In a similar method, the multi-feature absorption can be used to solve for up to n unknown characteristics (e.g. max or min temperature, boundary layer thickness, etc.) of a prescribed property profile based on CFD or theory. These techniques can become difficult in environments with complex non-uniformities or under situations of increased measurement noise. In addition, there is increased uncertainty when coupling these techniques with WMS because of the influence of spectral feature shape on WMS signals (which is avoided in the direct absorption measurements by using the integrated absorbance area of the spectral feature).

When multi-dimensional CFD solutions are available for comparison to LOS absorption measurements, the LOS path integration offers a different method to reduce the spatially-resolved CFD for direct comparison with the absorption measurements. In this method, which is shown schematically in Figure 8, the expected WMS signals are calculated from the CFD result along the laser LOS. The simulated WMS signals for the CFD result and the measured WMS signals in the scramjet are analyzed to yield a CFD LOS temperature and a laser-measured temperature; this method provides the density and line strength weighting needed for accurate comparison of the laser measurements with the CFD simulations.

As illustrated in the left panel of Figure 8, the temperature, pressure, H_2O and CO_2 mole fractions are first extracted from the CFD calculations for each volume element along the laser LOS that is used in the actual

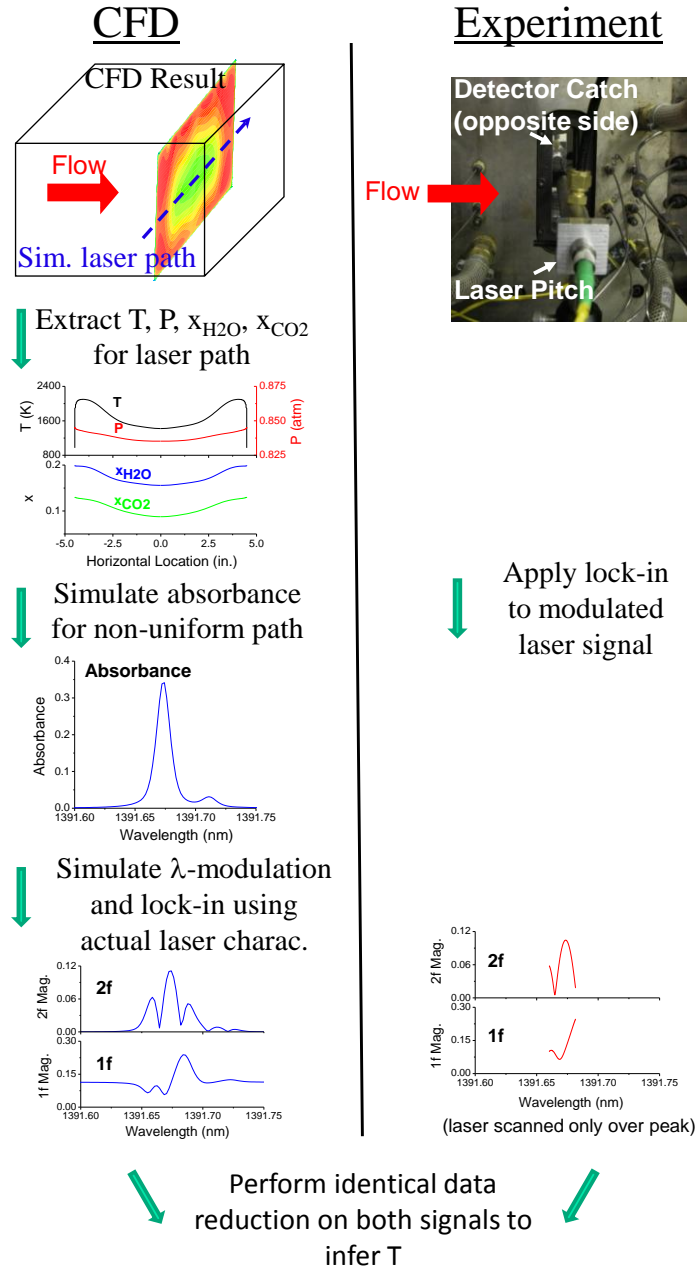


Figure 8. Method for comparison of multi-dimensional CFD with LOS laser measurement.

experiment. The absorbance on the laser-probed transition is calculated in each volume element and summed to determine the path-integrated CFD-predicted absorbance. The WMS models¹⁸ are used to simulate the CFD-predicted WMS-2f and -1f signals for both spectral features and the ratio of the predicted 1f-normalized WMS-2f signals is taken. Finally, both the predicted ratio and the actual measured ratio from the corresponding scramjet experiment are reduced to the predicted and laser-measured temperature.

E. Operating Conditions

Combustor inlet stagnation temperature was held fixed at $T_{VH} = 1390 \pm 5$ K while the stagnation pressure or fuel composition was varied as shown in Table 3. For each case shown in the table, the fuel-air equivalence ratio and the fuel distribution were also held constant ($\phi = 0.70$, $\phi_{B2} = 0.30$, $\phi_{B6} = \phi_{C3} = 0.20$). In each case listed, data from a single time slice were extracted from the nominally steady-state portion of the combustion test. These data were used to represent the performance and operability characteristics of each test case. In each case autoignition of the fuel was observed; no external aids (spark igniters, air throttles, or other means) were required to produce ignition or flame propagation in the combustor. Typically, combustion tests were run for more than 30 seconds to achieve steady-state conditions within the combustor. Occasionally, overheating of un-cooled portions of the combustor flowpath made it necessary to terminate the test before steady-state conditions were established.

Figure 9 shows time-based data collected from Case 1. Pressure and temperature data are shown from both air and fuel streams. Steady operating conditions are established prior to the introduction of fuel to the combustor. Fuel injection begins approximately 10 sec. into the experiment, as indicated by the changes in injection manifold conditions. Fuel injection pressures reach steady levels approximately 30 sec. into the test. Mass flow rate and load cell force data are also shown from the same experiment. The sudden increase in load cell force near 10 sec. corresponds to ignition. Steady force levels are achieved approximately 30 sec. into the test. Fuel is turned off at approximately 42 sec. followed by combustor flame out.

Table 3. Combustor operating conditions.

Case	Fuel	P_P0, MPa
1	C ₂ H ₄	1.72
2	C ₂ H ₄	1.30
3	60% C ₂ H ₄ + 40% CH ₄	1.72

III. Computational Approach and Tools

Simulations were performed using the CFD++ code, a general-purpose CFD tool developed by Metacomp Technologies.²⁵ CFD++ uses a finite-volume numerical framework, with multi-dimensional TVD schemes and Riemann solvers for accurate representation of supersonic flows. Multi-grid acceleration is available to provide a fast and accurate solution methodology for both steady and unsteady flows. Several one-, two-, and three-equation

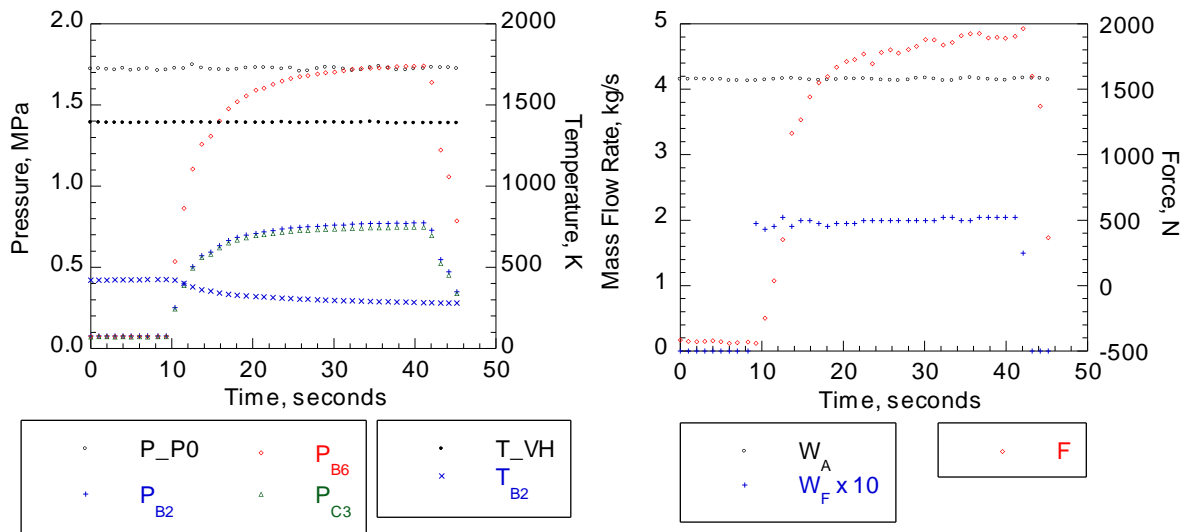


Figure 9. Time-based data from Case 1 (left: pressure and temperature, right: flow rate and force).

turbulence models are available for RANS calculations, along with large eddy simulation (LES) and hybrid RANS/LES options. Chemically reacting flows can be modeled with a general finite-rate kinetics model or a user-specified function for chemistry. The code supports both structured (quadrilateral and hexahedral) and unstructured (triangle, prism, and tetrahedral) grids. MPI is used to take advantage of modern parallel-processing computers. CFD++ has several types of Riemann solvers; the HLLC Riemann solver with Minmod flux limiting was used in the simulations described here. Turbulence was modeled with the two-equation cubic k - ϵ model, which has non-linear terms that account for normal-stress anisotropy, swirl, and streamline-curvature effects. At solid surfaces, an advanced two-layer wall function with the blended mode of equilibrium and non-equilibrium was employed to reduce grid requirements. The turbulent Schmidt (Sc_t) and Prandtl (Pr_t) numbers that control the modeled turbulent transport of mass and energy, respectively, were set to constant values. The value for Sc_t was calibrated to be 0.6 based on the comparison with experimental pressure distributions and the value for Pr_t was selected to be 0.9. Chemical kinetics were modeled using the reduced kinetic mechanism developed by Princeton University; it consists of 22 species and is based on the detailed mechanism of Wang and Laskin.²⁶

To accommodate the large grid sizes and the complex turbulence and combustion modeling, SGI Altix 4700 machines (96 parallel processors per simulation) at AFRL MSRC (a DoD High-Performance Computing Center) were utilized. For runs with combustion, ignition was achieved using a quasi-global ethylene reaction model and by reducing the activation energy by an order of magnitude. The reaction model was switched to the reduced kinetic mechanism once combustion became stable. For turbulent and reacting flows, mass balance is typically used as an indicator of solution convergence; all solutions were very steady and the mass-conservation errors across all boundaries were controlled below 0.1%. Except in the initial stage of the solution process, the CFL number was usually set to 5. To conserve CPU time, the initial solution of a typical simulation was normally chosen from the converged solution of a case with similar conditions. If a similar case was not available, a cold-flow solution without fuel injection (tare solution) was used as an initial solution.

Three-dimensional CFD data were reduced to equivalent one-dimensional results using the separated-flow averaging technique. This method uses two distortion terms and results in the preservation of mass, momentum, and energy flows along with the pressure force and kinetic energy flow while introducing little artificial entropy gain. In this method, the projected areas (A_i), mass flow (W), momentum flows (mom_i), total energy flow (E), pressure force in each direction (PA_i), and kinetic energy flow (KE) are determined by integrating the CFD solution. Species mass fractions are then determined from the ratio of each species flow to the total mass flow. The static pressure and enthalpy are found using Eqs. 8 and 9.

$$P = \frac{\vec{PA} \cdot \vec{A}}{\vec{A} \cdot \vec{A}} \quad (8)$$

$$h = \frac{E - KE}{W} \quad (9)$$

The density, temperature, and entropy are then determined using the equation of state that was used in the CFD solver. Next, the velocity components are found using Eq. 10.

$$U_i = \frac{mom_i - PA_i}{W} \text{ for } i = x, y, z \quad (10)$$

Finally, the extra distortion terms are found using the expressions in Eq. 11.

$$\eta_a = \frac{W}{\rho(\vec{V} \cdot \vec{A})}, \quad V_c = \frac{2KE}{W(\vec{V} \cdot \vec{V})} \quad (11)$$

Typically, the distortion terms remain near unity for non-separated flows. In these cases, the separated-flow averaging technique yields values that are very close to other averaging procedures. For separated flows like those encountered in shock trains and over cavity flameholders, the value of η_a decreases to mimic the actual flow area.

The combustion efficiency at the combustor exit is computed based on static enthalpy change using Eq. 12, where the reference condition is at the isolator entrance and the ideal condition is determined from an equilibrium calculation using the static pressure and static enthalpy at the combustor exit station.

$$\eta_{c,CFD} = \frac{h(T_{ref}, Y_{i,4}) - h(T_{ref}, Y_{i,ref})}{h(T_{ref}, Y_{i,ideal}) - h(T_{ref}, Y_{i,ref})} \quad (12)$$

IV. Results and Discussion

Combustor pressure distributions are used to examine the general operational characteristics of the combustor while combustion efficiency is used to describe overall combustor performance. OH-PLIF imaging is used to study the instantaneous and average characteristics of the reaction zone at an axial location just downstream of the cowl-side step flameholder. TDLAS provides quantitative measurements of temperature and water vapor concentration near the combustor exit plane. Each class of experimental results will be directly compared with results from corresponding computational simulations.

A. Combustor Operation and Performance

Pressure data reveal the location of the pre-combustion pressure rise, which accompanies dual-mode combustor operation, as well as the regions of high heat release (inferred from regions of locally high static pressures). Combustion efficiency is a global measure of the amount of fuel consumed (experimental) or enthalpy rise (computational) during the combustion process relative to an ideal condition where all fuel is consumed.

Figure 10 presents pressure distributions from Case 1. Combustor static pressure data measured on all four walls of the flowpath are scaled using the combustor inlet mass flux (ρU) and the axial position is scaled by the combustor throat height (H). Flowpath lines and pressure measurements from tare conditions ($\phi = 0$) are included for reference. The computational results include data from the body, cowl, and sidewall centerlines as well as one-dimensionally-averaged pressures through the combustor. Two regions of high pressure are apparent in the experimental data during combustion: one near the primary cavity flameholder and another downstream of the step flameholders. The combustor is operating in dual-mode as evidenced by the pre-combustion shock train positioned within the isolator portion of the flowpath (pressure rise begins near $x/H = 4$ for this case). The 1D CFD results closely reproduce the shock train position and the characteristics of the pressure distribution downstream of $x/H = 16$. However, the CFD results significantly underpredict the peak pressure associated with the primary flameholder. The experimental data from body, cowl, and sidewalls collapse very well in the isolator and cavity regions and show a monotonic increase in the downstream direction. The CFD results from the body and cowl walls exhibit evidence of shock wave interactions resulting in the oscillatory pressure distributions shown. The data from the sidewall, however, show a smooth rise in pressure similar to the experimental data.

Figure 11 and Figure 12 show similar characteristics resulting from Cases 2 and 3, respectively. In both of these plots, only the 1D CFD results are included for clarity. These results closely capture the pre-combustion shock train position and the characteristics of the combustor flowfield downstream of the body- and cowl-side step flameholders observed in the experiments, while the peak pressure in the vicinity of the primary flameholder is underpredicted. Based on the similarity of the three sets of results, it can be concluded that variations in combustor inlet stagnation

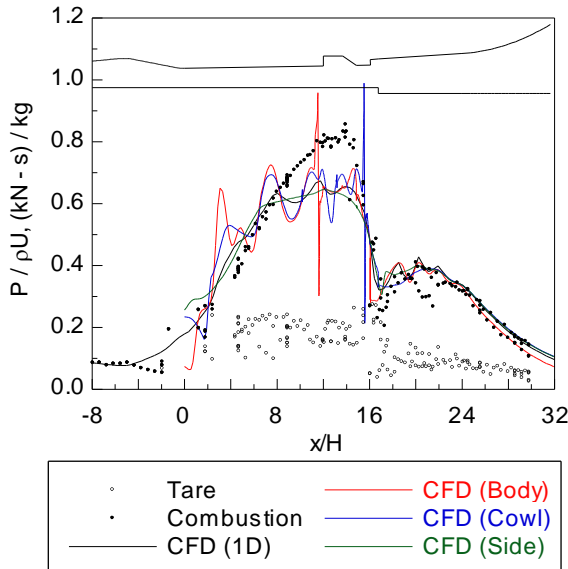


Figure 10. Pressure distributions from Case 1.

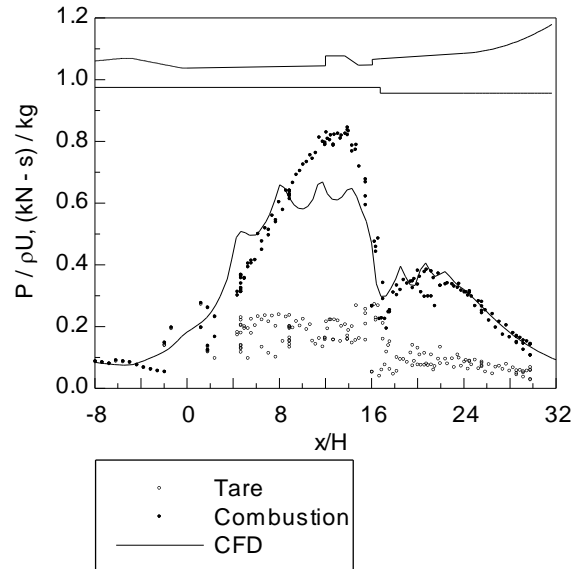


Figure 11. Pressure distribution from Case 2.

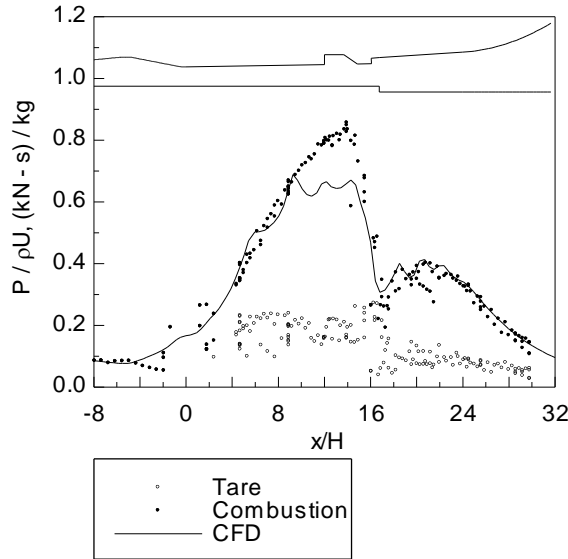


Figure 12. Pressure distributions from Case 3.

turbulence model selection. Third, the wall heat transfer may have an influence on the ability to accurately predict the pressure rise near the cavity flameholder. For example, an adiabatic wall assumption will result in a different pressure and temperature near the flameholder than will an isothermal wall assumption. Finally, the kinetic model can have an influence in this part of the flowfield.

Table 4 contains combustion efficiency results from both the experiments and the computational simulations. In each case, the computations predict 10-20% higher combustion efficiencies than those determined in the experiments. One contributor to this difference is associated with the different combustion efficiency definitions used (Equations 6 and 12, respectively). It is also possible that the CFD models overpredict heat release leading to higher temperature and water vapor concentration at the combustor exit.

B. OH Distributions

Figure 13 through Figure 15 show distributions of the OH radical, in a linear 8-bit gray scale, obtained from both experiment and computational simulation for Cases 1 – 3, respectively. In both sets of results, the flow direction is out of the page with the combustor sidewall at the right hand side of the images. The experimental data show ensemble-averaged images obtained by averaging the 180 instantaneous images. Each experimental image has the same range of gray scales to allow objective comparison. Light regions indicate high concentrations of OH, while darker regions indicate reduced concentrations of OH. Hydroxyl on the right side of the image absorbs laser

Table 4. Combustor performance.

Case	$\eta_{C,YF}$	$\eta_{C,CFD}$
1	0.75	0.89
2	0.78	0.91
3	0.77	0.87

pressure or fuel selection have a small impact on the overall operation of the combustor for the range of variations considered in these experiments (see Table 3).

Several factors may influence the CFD results, especially in the region near the cavity flameholder where the flowfield is subject to unsteadiness. First, the RANS solution scheme is inherently limited in its ability to solve unsteady flow problems such as this. Second, turbulence modeling remains a source of uncertainty within RANS CFD codes. These models dictate the level of turbulent diffusion associated with fuel-air mixing and are often very problem-specific. The prediction of shock-boundary layer interactions is also strongly influenced by the

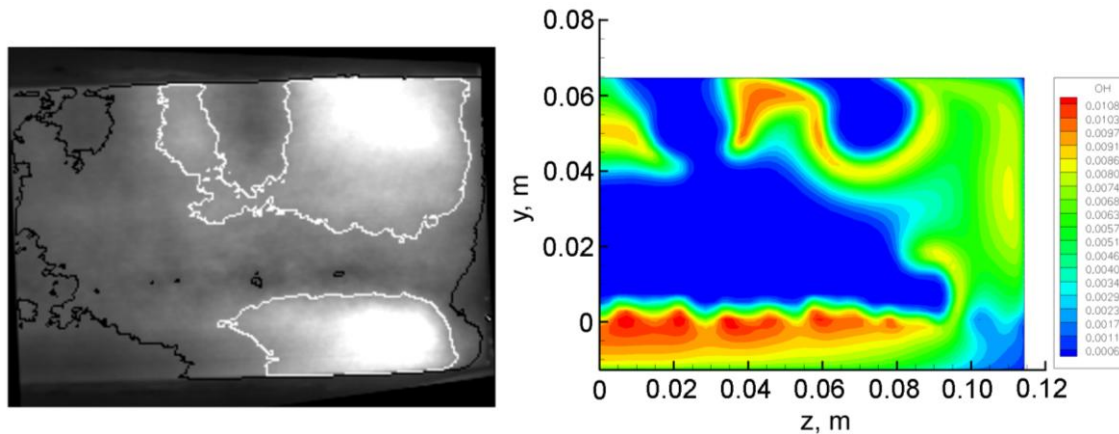


Figure 13. Average experimental (left) and computational (right) OH distributions for Case 1.

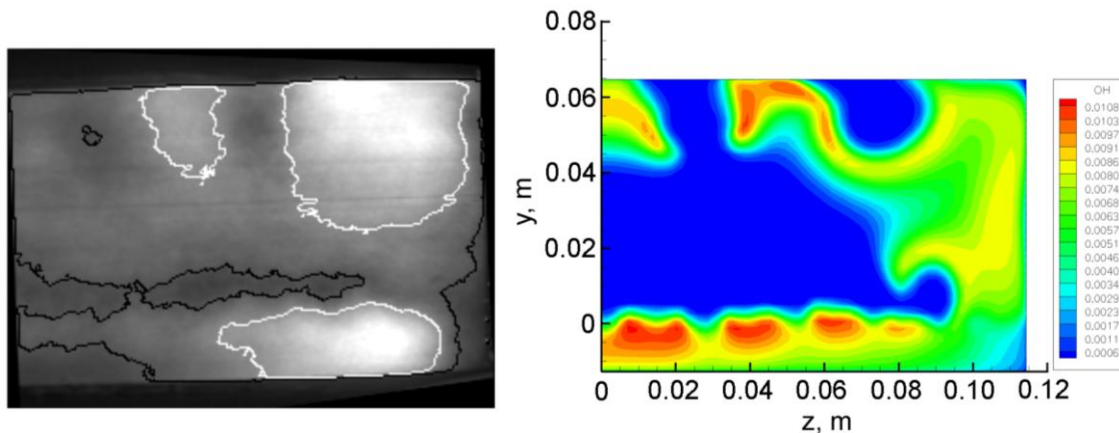


Figure 14. Average experimental (left) and computational (right) OH distributions for Case 2.

energy, thereby decreasing the signal on the left side. Also, the left side of the image is more strongly affected by fluorescence trapping. Two arbitrary contours are shown in the experimental data (same contour levels for each figure) to minimize subjectivity. A color scale is included with the computational data to indicate the OH concentration (blue regions contain essentially no OH while red regions contain the highest concentrations of OH).

In Figure 13, the experimental data reveal high concentrations of OH in the body/sidewall corner, along the sidewall, and in the cowl step flameholder regions. Generally, OH is present throughout the field of view, although two darker regions associated with the fuel-rich plumes of the B6 injectors can be observed near the body wall of the combustor. The computational result shows similar features, although there are some interesting differences as well. The importance of the body/sidewall corner, sidewall, and cowl step flameholder regions is clear from the CFD result. The region of high OH concentration near the sidewall is contained in a very thin layer at this condition ($P_{P0} = 1.72$ MPa). Donbar, et al.⁵ observed the sidewall OH region near the cavity flameholder to be very thin at high dynamic pressures and substantially broader at lower dynamic pressures. The fuel-rich plumes associated with the B6 injectors are also obvious in the CFD solution (blue regions near the body wall). The CFD result shows the OH region downstream of the cowl side step flameholder to be relatively uniform except for the influence of the C3 fuel injectors. Very low levels of OH are predicted in the core flow region compared with the experimental data, and the B6 fuel plumes appear to be pushed toward the combustor sidewall relative to the plumes observed in the experimental data. Also, the CFD shows much more OH than does the PLIF measurement in the region around the midpoint of the sidewall. Based on the comparison between the experimental and computational results, it appears that the CFD combustion model overpredicts the rate of OH recombination. This may be influenced by the turbulence modeling (through the rate of turbulent diffusion) and/or the combustion kinetic model.

Results from Case 2 (Figure 14) show many characteristics similar to those in Case 1. In this case, the dynamic pressure is lower ($P_{P0} = 1.30$ MPa) but the fuel distribution, equivalence ratio, and fuel composition are unchanged. The computational results show broader regions of high OH concentration. For example, the CFD result near the sidewall shows a much larger region containing high levels of OH. As noted earlier, this result is in agreement with previous OH-PLIF imaging results.⁵

CFD results are also shown from Case 3 in Figure 15. The OH distribution is very similar in structure to the other two cases, although concentrations in the body and sidewall regions are somewhat lower. The cowl step flameholder region remains relatively uniform and the influence of the individual fuel injectors at the C3 station persists.

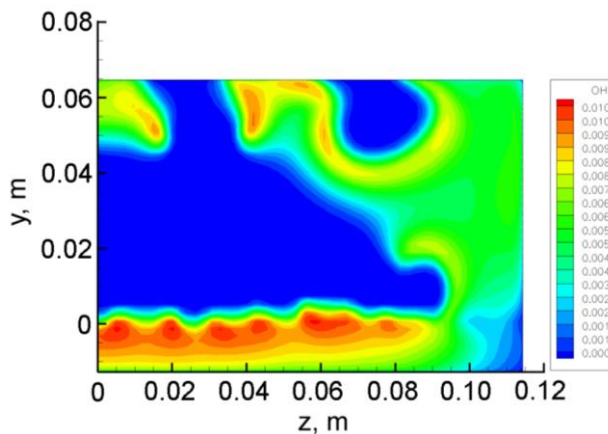


Figure 15. Computational OH distributions for Case 3.

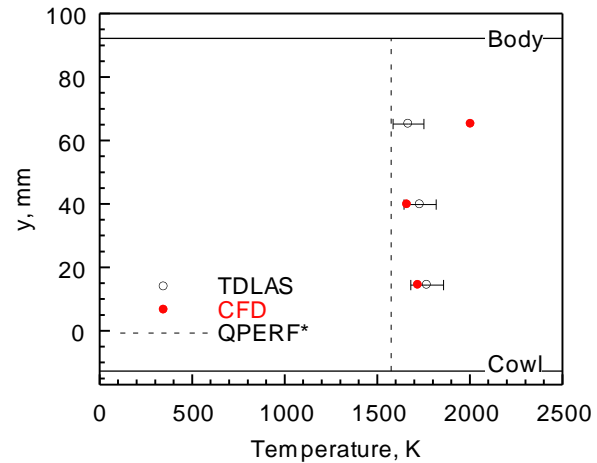
C. Static Temperature and Water Vapor Concentration Profiles

A plane of data from the TDLAS measurement location (see Figure 1) was extracted from each CFD simulation. Using the analysis procedure described in Figure 8, the 2D CFD data were reduced to provide static temperatures and water mole fractions for direct comparisons with the TDLAS measurements. The uncertainty associated with the comparison between the predicted and laser-measured temperature and water concentration is represented by uncertainty bars on the TDLAS results (shown in the following figures). The uncertainty bars are the compound result of the uncertainty in the spectral model, and the effects of potential variation in pressure and mole fraction between the CFD and actual values. They represent uncertainty levels of $\pm 4.6\%$ in the temperature measurements and $\pm 5.3\%$ in the concentration measurements. The QPERF results were used to determine 1D values of static temperature and water vapor mole fraction at the combustor exit plane. Although the physical location corresponding to the QPERF results is downstream of the TDLAS measurement location (refer to Figure 1), these values are included to provide a reasonable bound for comparison purposes. The temperature data resulting from this analysis are expected to have lower values than those from the upstream TDLAS location because of supersonic flow acceleration in the diverging channel and heat loss through the cooled combustor walls.

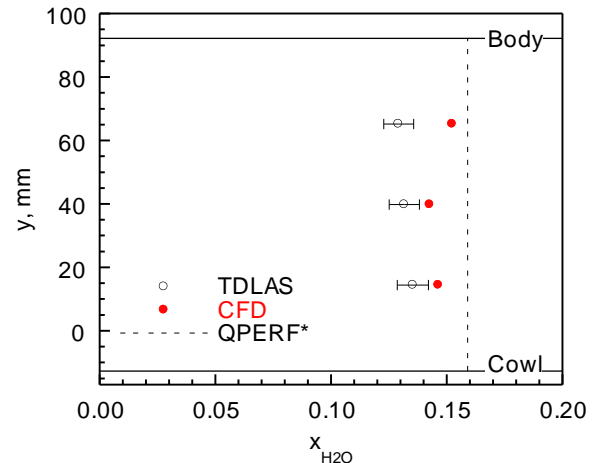
Figure 16 presents the three sets of results for both static temperature and water vapor concentration from Case 1. Shown in the plots for reference are the body and cowl wall locations. In this case, three measurement locations were examined in the core-flow region of the combustor. The static temperature measurements shown in Figure 16a agree closely (within about 4%) with the CFD predictions below the $y = 40$ mm location. Above this location, the measured temperature is about 20% lower than predicted. The 1D QPERF result is substantially lower than both the CFD and TDLAS results as expected. Figure 16b shows the water vapor concentrations obtained from the three methods. The CFD simulations predict higher levels of water vapor across the combustor height than the measured values. This is consistent with the combustion efficiency data presented in Table 4 that showed the CFD predicting higher levels of combustion than the experiment.

Nine vertical positions were examined with the diode laser measurement in Case 2. Figure 17 presents the temperature and concentration profiles from this case. The static temperature measurements and CFD results (Figure 17a) reveal locally high temperature regions nearest the body and cowl walls and a relatively cool region in the core flow. As with the results from Case 1, excellent agreement between the numerical predictions and the measurements occurs in the core region of the combustor (between $y = 0$ and 50 mm) while in the near-wall regions, the CFD results predict higher static temperatures. The 1D static temperature from the combustor exit plane closely matches the measurements and CFD in the core region, but is lower than both data sets near the walls.

Figure 17b presents the water vapor concentrations from Case 2. Both the CFD and the diode laser measurement indicate that the water concentration is non-uniform across the combustor height, where higher concentrations of water are found in the regions of high static temperature near the combustor walls. The measurements and CFD results reveal similar profiles, with the CFD again overpredicting the level of water present at the measurement location. Together, these trends in temperature and water concentration suggest



(a) Static temperature.



(b) Water vapor mole fraction.

Figure 16. Static temperature and water vapor concentration profile data from Case 1 (*QPERF results are from a plane downstream of both the TDLAS and CFD results).

that the CFD results underpredict the degree of turbulent mass and energy transport. As in Case 1, the QPERF results indicate higher water concentrations than either the TDLAS or the CFD results.

For Case 3, only two vertical positions were interrogated with the diode laser sensor (one point near the vertical centerline and one point in the lower half of the combustor). Figure 18 presents the temperature and water concentration results. Similar trends are observed among the three sets of results. Close agreement between the TDLAS and CFD results in this region of the flowfield is again observed. The 1D QPERF results from the combustor exit plane again show a lower static temperature (as expected) and a higher water concentration.

A simple path-averaged temperature was also determined from the CFD result for Case 2 to compare with the results from the reduction algorithm described in Figure 8. These results are shown in Figure 19. In this case, the path-averaged temperature does not reflect the influence of the variations in the thermodynamic properties or species concentration along the line-of-sight on the temperature measured by laser absorption – it is purely a spatially-averaged temperature. It is immediately observed that both the path-averaged temperature and the temperature deduced using the TDLAS data reduction algorithm demonstrate the same non-uniform distribution across the combustor height at this flowfield station. The path-averaged temperature is slightly higher primarily because of the increased sensitivity of the laser measurement to the cooler regions in the flow. Based on this analysis, the temperature measurements obtained from the TDLAS sensor should reflect the trend of the path-averaged temperature.

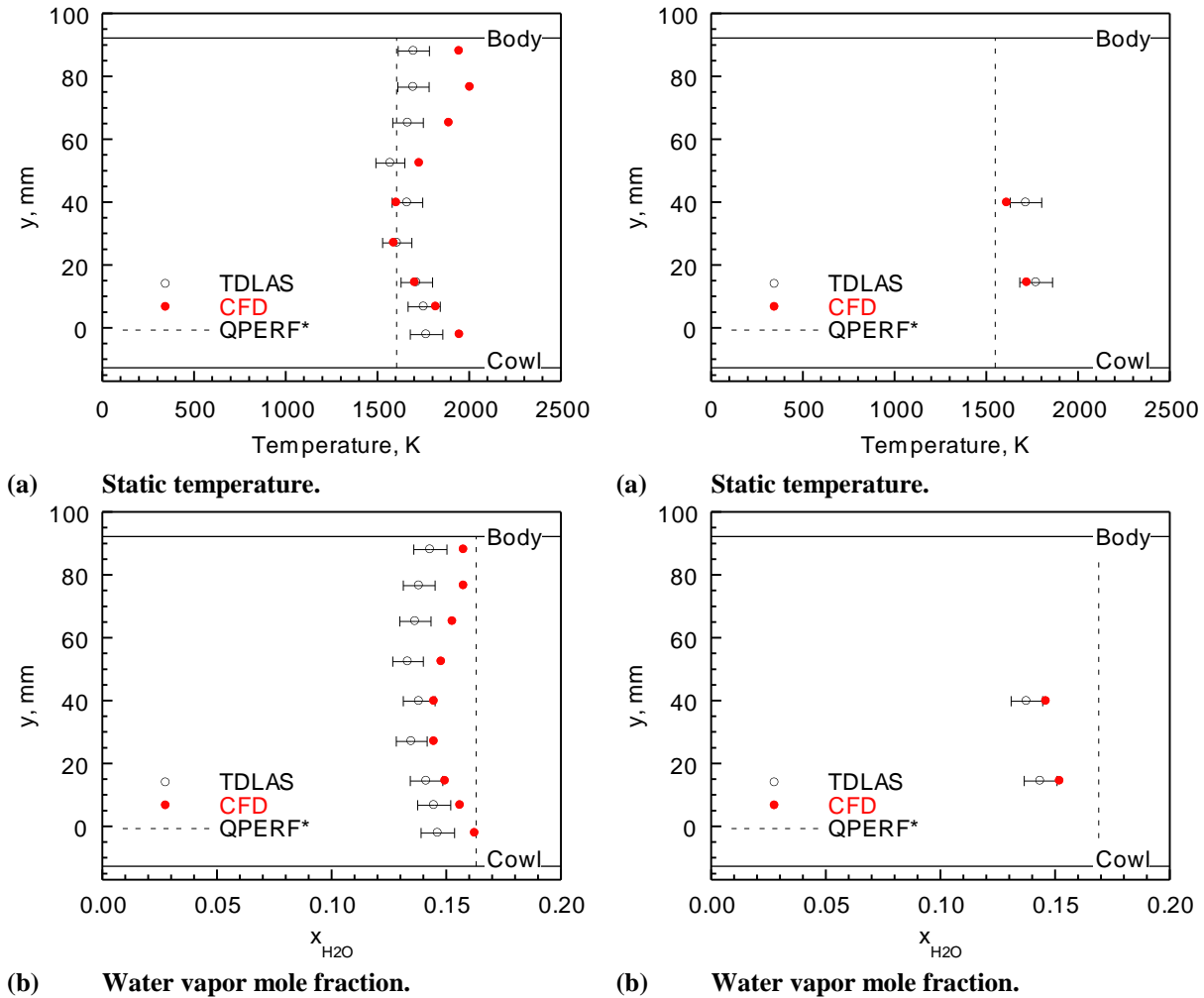


Figure 17. Static temperature and water vapor concentration profile data from Case 2 (*QPERF results are from a plane downstream of both the TDLAS and CFD results).

Figure 18. Static temperature and water vapor concentration profile data from Case 3 (*QPERF results are from a plane downstream of both the TDLAS and CFD results).

V. Summary

Laser-based measurements were successfully employed in a hydrocarbon-fueled supersonic combustor. Both planar (OH-PLIF) and line-of-sight (TDLAS) diagnostic techniques were performed. These measurements were combined with conventional instrumentation and CFD to obtain assessments of combustor operational and performance characteristics. In these experiments the combustor was fueled at a fixed fuel-air ratio and fuel distribution with both ethylene and a mixture of ethylene and methane. Combustor inlet conditions simulated flight at approximately Mach 5.5 at two dynamic pressures.

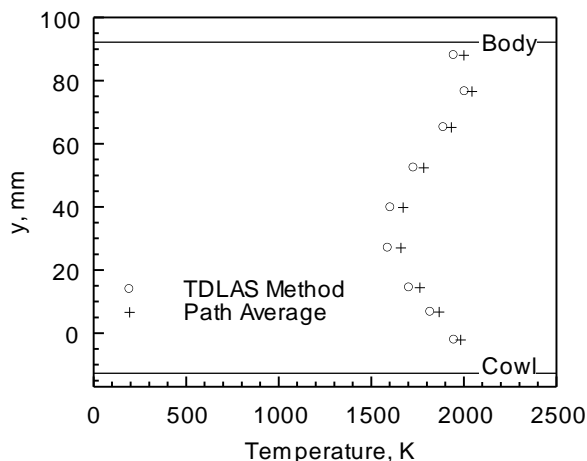


Figure 19. Comparison of CFD static temperature data reduced using the TDLAS approach and a simple path average.

- Pressure distributions reveal two regions of elevated static pressure in the combustor. The first region is associated with combustion near the cavity flameholder. The second region occurs farther downstream and is caused by heat release in the step flameholder region. For the conditions in this study, the combustor operates in dual-mode with a pre-combustion shock train positioned in the isolator region of the flowpath. The computational simulations compare reasonably well with the experimental results except for an underprediction of the primary pressure peak.
- The CFD simulations predict higher levels of combustion efficiency than are measured. The combustion efficiency definitions are slightly different, which may account for some of the difference between the two sets of data. This topic is currently under further investigation.
- The experimental and computational OH distributions indicate the importance of the sidewall region in providing a flame propagation path from the body to the cowl side combustion zones. These distributions also show the effectiveness of the cowl-side step flameholder. The experimental results indicate that OH is generally more distributed throughout the flowfield than predicted by CFD. This observation suggests that the CFD models overpredict the conversion rate of OH to H₂O which may be influenced by the turbulence and/or kinetic modeling. Such insights are generally not available from conventional instrumentation alone.
- A new approach has been developed for comparing line-of-sight absorption measurements with multi-dimensional CFD calculations based on analyzing the CFD results using the same algorithm as used in the TDLAS experiments. This approach incorporates the appropriate spectroscopic influences using the local thermodynamics from the CFD solution to produce “simulated absorption” signals from the multi-dimensional CFD results. These “simulated absorption” signals are then processed using the TDLAS data reduction algorithm to yield static temperature and water vapor concentration results for direct comparison with the experimental results.
- Analyzing the CFD results using the TDLAS methodology does not appear to introduce any confounding artifacts compared with simply using a path-averaged temperature. In other words, the temperature distributions obtained from the CFD results using TDLAS data reduction and path-averaging compare quite well, suggesting that the measurements reflect the actual path-averaged temperature.
- The TDLAS measurements reveal the body-to-cowl temperature and water concentration profiles. The distributions of these quantities at the measurement plane are non-uniform across the vertical dimension of the combustor. CFD and TDLAS temperature results compare closely in the core flow region of the combustor (within 5%) but show poorer agreement near the combustor walls. The measurements of water vapor concentration are lower than predicted by the CFD model at every position across the height of the

combustor. Together, these results suggest that the CFD may underpredict turbulent mass/energy transport as well as overpredict the rate of OH to H₂O conversion. Such insights are generally not available from conventional instrumentation alone.

Acknowledgments

The authors acknowledge the combined energies of the AFRL/RZA management (Mr. P. Buckley, Dr. T. Jackson, and Mr. R. Mercier) for their financial and technical support of this effort. AFOSR funding (Dr. Julian Tishkoff as monitor) allowed the diode laser and OH-PLIF measurements to be made. The computational resources for this project were provided by the DoD High Performance Computing Modernization Office at the ASC Major Shared Resource Center. Finally, the authors acknowledge the contributions of Mr. J. Diemer, Mr. W. Haendiges, Mr. R. Ryman, Mr. C. Smith, Mr. S. Smith, and Mr. G. Streby for technical and operational support of the experimental research facility. Support of the AFRL/RZ Research Air Facility is also appreciated.

References

- ¹Ben-Yakar, A., and Hanson, R. K., "Hypervelocity Combustion Studies Using Simultaneous OH-PLIF and Schlieren Imaging in an Expansion Tube," AIAA Paper 99-2453, June 1999.
- ²Hartfield, R. J., Hollo, S. D., and McDaniel, J. C., "Experimental Investigation of a Supersonic Swept Ramp Injector Using Laser-Induced Iodine Fluorescence," *Journal of Propulsion and Power*, Vol. 10, No. 1, 1994, pp. 129-135.
- ³Gruber, M. R., Donbar, J. M., Carter, C. D., and Hsu, K.-Y., "Mixing and Combustion Studies Using Cavity-Based Flameholders in a Supersonic Flow," *Journal of Propulsion and Power*, Vol. 20, No. 5, 2004, pp. 769-778.
- ⁴O'Byrne, S., Stotz, I., Neely, A. J., Boyce, R. R., Mudford, N. R., and Houwing, A. F. P., "OH PLIF Imaging of Supersonic Combustion using Cavity Injection," AIAA Paper 2005-3357, May 2005.
- ⁵Donbar, J. M., Gruber, M. R., Jackson, T. A., Carter, C. D., and Mathur, T., "OH Planar Laser-Induced Fluorescence Imaging in a Hydrocarbon-Fueled Scramjet Combustor," *The 28th Symposium (International) on Combustion*, The Combustion Institute, Pittsburgh, 2000, pp. 679-687.
- ⁶Allen, M. G., Upschulte, B. L., Sonnenfroh, D. M., Kessler, W. J., and Mulhall, P. A., "Overview of Diode Laser Measurements in Large-Scale Test Facilities," AIAA Paper 2000-2452, June 2000.
- ⁷Liu, J. T. C., Jeffries, J. B., Hanson, R. K., Creighton, S., Lovett, J. A., and Shouse, D. T., "Diode Laser Absorption Diagnostics for Measurements in Practical Combustion Flow Fields," AIAA Paper 2003-4581, July 2003.
- ⁸Liu, J. T. C., Jeffries, J. B., and Hanson, R. K., "Wavelength Modulation Absorption Spectroscopy with 2f Detection for Combustion Temperature Measurements Using Multiplexed Near-Infrared Diode Lasers," AIAA Paper 2004-0647, January 2004.
- ⁹Liu, J. T. C., Rieker, G. B., Jeffries, J. B., Hanson, R. K., Gruber, M. R., Carter, C. D., and Mathur, T., "Near-Infrared Diode Laser Absorption Diagnostic for Temperature and Water Vapor in a Scramjet Combustor," *Applied Optics*, Vol. 44, No. 31, 2005, pp. 6701-6711.
- ¹⁰Rieker, G., Liu, J., Jeffries, J., Hanson, R., Mathur, T., Gruber, M., and Carter, C., "Diode Laser Sensor for Gas Temperature and H₂O Concentration in a Scramjet Combustor Using Wavelength Modulation Spectroscopy," AIAA Paper 2005-3710, July 2005.
- ¹¹Rieker, G. B., Jeffries, J. B., Hanson, R. K., Mathur, T., Gruber, M. R., and Carter, C. D., "Diode Laser-Based Detection of Combustor Instabilities with Application to a Scramjet Engine," accepted to Proceedings of the Combustion Institute, Vol. 32, 2008.
- ¹²Williams, S., Barone, D., Barhorst, T., Jackson, K., Lin, K.-C., Masterson, P., Zhao, Q., and Sappey, A. D., "Diode Laser Diagnostics of High Speed Flows," AIAA Paper 2006-7999, November 2006.
- ¹³Lindstrom, C., Tam, C.-J., Davis, D., Eklund, D., and Williams, S., "Diode Laser Absorption Tomography of 2D Supersonic Flow," AIAA Paper 2007-5014, July 2007.
- ¹⁴Gruber, M., Donbar, J., Jackson, K., Mathur, T., Baurle, R., Eklund, D., and Smith, C., "Newly Developed Direct-Connect High-Enthalpy Supersonic Combustion Research Facility," *Journal of Propulsion and Power*, Vol. 17, No. 6, 2001, pp. 1296-1304.
- ¹⁵Gruber, M. R., Hagenmaier, M. A., and Mathur, T., "Simulating Inlet Distortion Effects in a Direct-Connect Scramjet Combustor," AIAA Paper 2006-4680, July 2006.
- ¹⁶Donbar, J., Powell, O., Gruber, M., Jackson, T., Eklund, D., and Mathur, T., "Post-Test Analysis of Flush-Wall Fuel Injection Experiments in a Scramjet Combustor," AIAA Paper 2001-3197, July 2001.

- ¹⁷Smith, S., Schied, A., Eklund, D., Gruber, M., Wilkin, H., and Mathur, T., "Supersonic Combustion Research Laboratory Uncertainty Analysis," AIAA Paper 2008-5065, July 2008.
- ¹⁸Li, H., Rieker, G. B., Liu, X., Jeffries, J. B., and Hanson, R. K., "Extension of Wavelength-Modulation Spectroscopy to Large Modulation Depth for Diode Laser Absorption Measurements in High-Pressure Gases," *Applied Optics*, Vol. 45, No. 5, 2006, pp. 1052-1061.
- ¹⁹Rieker, G. B., Jeffries, J. B., and Hanson, R. K., "Calibration-Free Wavelength Modulation Spectroscopy for Harsh, Non-Uniform Environments," in preparation.
- ²⁰Uehara, K. and Tai, H., "Remote Detection of Methane with a 1.66 μm Diode Laser," *Applied Optics*, Vol. 31, No. 6, 1992, pp. 809-814.
- ²¹Fernholz, T., Teichert, H., and Ebert, V., "Digital, Phase-Sensitive Detection for In Situ Diode-Laser Spectroscopy Under Rapidly Changing Transmission Conditions," *Applied Physics B*, Vol. 75, 2002, pp. 229-236.
- ²²Seitzman, J. M. and Scully, B. T., "Broadband Infrared Absorption Sensor for High-Pressure Combustor Control," *Journal of Propulsion and Power*, Vol. 16, No. 6, 2000, pp. 994-1001.
- ²³Sanders, S. T., Wang, J., Jeffries, J. B., and Hanson, R. K., "Diode-Laser Absorption Sensor for Line-of-Sight Gas Temperature Distributions," *Applied Optics*, Vol. 40, No. 24, 2001, pp. 4404-4415.
- ²⁴Liu, X., Jeffries, J. B., and Hanson, R. K., "Measurement of Nonuniform Temperature Distributions Using Line-of-Sight Absorption Spectroscopy," *AIAA Journal*, Vol. 45, No. 2, 2007, pp. 411-419.
- ²⁵Metacomp, CFD++, Metacomp, <http://www.metacomptech.com/index.html>, 2006.
- ²⁶Wang, H. and Laskin, A., "A Comprehensive Kinetic Model of Ethylene and Acetylene Oxidation at High Temperature," Internal Report for an AFOSR New World Vista Program, 1998.